Hindawi Publishing Corporation
Journal of Spectroscopy
Volume 2015, Article ID 836859, 9 pages
http://dx.doi.org/10.1155/2015/836859

Research Article

$ZnO/ZnAl_2O_4$ Nanocomposite Films Studied by X-Ray Diffraction, FTIR, and X-Ray Photoelectron Spectroscopy

S. Iaiche[1,2] and A. Djelloul[1]

[1]*Laboratory of Structures, Proprieties and Inter Atomic Interactions University, 40000 Khenchela, Algeria*
[2]*Department of Materials Science, Faculty of Science, Larbi Ben M'hidi University, 04000 Oum El Bouaghi, Algeria*

Correspondence should be addressed to A. Djelloul; djelloulabdelkader@yahoo.fr

Received 8 February 2015; Revised 27 March 2015; Accepted 6 April 2015

Academic Editor: Rizwan Hasan Khan

$ZnO/ZnAl_2O_4$ nanocomposite films were synthesised by ultrasonic spray pyrolysis (USP) by extracting $Al_2O(SO_4)_2$ oxide with zinc chloride hydrate in deionised water. The sample was then subjected to heat treatment at 650°C and 700°C for 1 h, which led to the formation of the spinel oxide ($ZnAl_2O_4$) and wurtzite (ZnO) phases. $Al_2(SO_4)_3{\cdot}18H_2O$ salt was transformed into aluminum oxide sulfate $Al_2O(SO_4)_2$, which is an intermediary decomposition product, by calcination at 795°C for 3 h. The structures of the synthesised $ZnO/ZnAl_2O_4$ films were confirmed by XRD, FTIR, and X-ray photoelectron spectroscopy (XPS). XPS spectra of the major Zn, Al, and O photoelectron lines and the major X-ray induced Zn LMM Auger lines for $ZnO/ZnAl_2O_4$ are presented.

1. Introduction

Zinc aluminate ($ZnAl_2O_4$) is of interest due to its desirable properties, such as its high mechanical resistance, high thermal stability, low-temperature sinterability, low surface acidity, and good diffusion [1]. These characteristics make it very suitable for applications as a high-temperature material, catalyst, catalyst support, ceramic pigment, and optical and thermal control coating for spacecraft, and it is emerging as one of the best wide-band-gap compound semiconductors (E_g = 3.8 eV) for UV optoelectronic applications [2]. In addition, $ZnAl_2O_4$ is also widely used in many catalytic reactions, cracking, dehydration, hydrogenation, pollution control, and dehydrogenation [3, 4]. According to Hadnadev-Kostić et al., the calcination of ZnAl layered double hydroxides leads to the formation of high-photocatalytic-activity mixed ZnO-$ZnAl_2O_4$ oxides with high surface area and thermal stability. This enhancement of the photocatalytic behaviour is due to the presence of the ZnO semiconductor (E_g = 3.2 eV), which has a photocatalytic potential assigned to its activation in the visible region and the presence of the spinel phase [5].

This letter is a contribution to the simplest preparation methods for mixed oxides. The $ZnO/ZnAl_2O_4$ system has been successively prepared by a USP method employing $Al_2(SO_4)_3{\cdot}18H_2O$ salt as a new precursor for the $ZnAl_2O_4$ phase. We also attempt to determine the appropriate synthesis conditions in terms of the substrate and annealing temperatures for the formation of composite films. This paper also presents the XPS spectra of the major Zn, Al, and O photoelectron lines and the major X-ray induced Zn LMM Auger lines for $ZnO/ZnAl_2O_4$.

2. Experimental

Aluminium sulphate hydrate salt was used as the Al metal source in our synthesis. For this purpose, different calcination temperatures in the range of 750 to 1200°C were applied to $Al_2(SO_4)_3{\cdot}18H_2O$ initial powder to induce its thermal decomposition. We have chosen to report the analysis of the 785 and 795°C treatments in this study. The calcination was carried out in air atmosphere for 3 h. The spraying solution was 0.06 M in zinc chloride dihydrate ($ZnCl_2{\cdot}2H_2O$) and 0.12 M in the calcination final product with distilled water as the solvent. This solution was maintained under constant-temperature (below 100°C) agitation for 8 h. Magnetic stirrer agitation promoted the chemical reaction between precursors, facilitating the dissolution of the salts in water and maintaining the high homogeneity of the solution. The ultrasonic

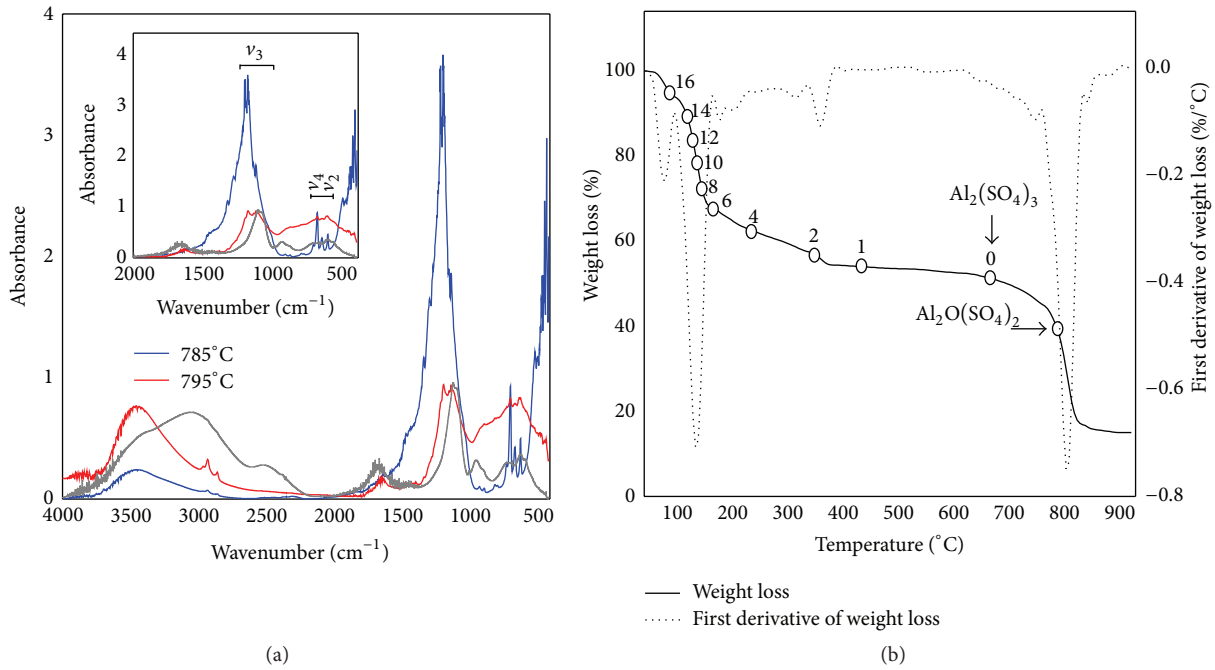

FIGURE 1: FTIR absorption spectrum of the calcination products (3 h, 785 or 795°C) of $Al_2(SO_4)_3 \cdot 18H_2O$ powder and that of $Al_2(SO_4)_3 \cdot 18H_2O$ powder for comparison (grey line) (the main bands are discussed in the text) (a) and thermogravimetric (TG) curve for $Al_2(SO_4)_3 \cdot 18H_2O$ at 5°C/min (b). The theoretical number of water molecules and weight loss associated with each $Al_2(SO_4)_3$ unit are given.

spraying system used in this work consists of a commercial ultrasonic atomizer VCX 134 AT and a substrate holder with heater. The ultrasonic vibrator frequency was 40 kHz and the power used was 130 W. The median drop size at 40 kHz is 45 μm. The nozzle-substrate distance was 5 cm and, during the deposition, the solution flow rate was held constant at 0.2 mL/min. The substrate (quartz) temperature (Ts) during deposition was 570°C, and the deposition time was fixed at 30 min. After deposition, the sample was annealed in air for 1 h at 650°C and 700°C.

The crystalline structure of the deposited specimen was determined by X-ray diffraction (XRD) with a radiation wavelength of 1.5418 Å (CuK_α). The chemical bonding states of the as-calcined powder or the films obtained were characterised by Fourier-transform infrared spectrometry (Nicolet 460 FTIR) at room temperature. The sample for FTIR measurements was prepared by grinding the film scraped from the quartz substrate. The uncertainty in the position of the various peaks is ±2 cm^{-1}. The thermogravimetric (TG) data were recorded under a dry air flow with a heating rate of 5°C/min in a SETARAM TGDTA92 16.18 thermal analyser. TG measurements were corrected for temperature-dependent buoyancy by subtracting the data of a measurement carried out on an inert sample. The X-ray photoelectron spectroscopy (XPS) analysis was carried out with a PHI 5000 VersaProbe-Scanning ESCA Microprobe using monochromatized Al K_α X-ray source ($h\nu$ = 1486.6 eV, 15 kV, 39.3 W, diameter beam spot: 200 μm) by calibrating binding energy to C1s (285.1 eV). The surface contaminants were removed by means of mild sputtering method using 2 kV Ar^+ ions.

3. Results and Discussion

Figure 1(a) illustrates the FTIR patterns of the intermediate products of the 3-h calcination of the aluminium sulphate hydrate powder at 785 or 795°C. The spectra present some notable differences related to the molecular and structural bonding states of the calcined powder. Three bands are assigned to the ν_3 (SO_4^{2-}) mode for the salt heated at 785°C: 1150, 1181, and 1250 cm^{-1}. The SO_4^{2-} group in sulphate minerals can exhibit four infrared-active vibrational modes, including a strong F antisymmetric bend (ν_3) and a generally weak E symmetric bend (ν_2). These vibrational bands generally occur as two to four ν_3 bands between 960 and 1280 cm^{-1} and one or two ν_2 bands between 420 and 525 cm^{-1} [7]. The weaker ν_2 vibration band appears at approximately 500 cm^{-1}. It should be noted that the principal changes in the FTIR spectra are observed in the bands located between 584 and 712 cm^{-1}. Indeed, the FTIR curve of aluminium sulphate hydrate calcined at 785°C includes additional characteristic triplet absorption bands at 584–712 cm^{-1} compared to the spectrum of that calcined at 795°C. These bands can be attributed to vibrations of the $(Al\text{-}O\text{-}Al)^{4+}$ group [8]. Additionally, the FTIR patterns of calcined powders exhibit a band at 3443 cm^{-1} and a weak band at 1638 cm^{-1}, which are assigned to the vibration mode of chemically bonded hydroxyl groups and the deformation vibration of water molecules, respectively. Three peaks of very weak intensities at 2856 cm^{-1}, 2927 cm^{-1}, and 2960 cm^{-1} are attributed to the C–H stretching vibrations of alkane groups [9].

The thermal decomposition of aluminium sulphate hydrate is a possible means for the production of high-purity aluminium oxides with fine grains via intermediate steps [10]. Alumoxane cations (Al_2O^{4+}) from aluminum oxide sulfate $Al_2O(SO_4)_2$ and sulphite ions (SO_3^{2-}) are present in the intermediate products formed during the thermal decomposition of $Al_2(SO_4)_3{\cdot}18H_2O$ [8].

Figure 1(b) shows the typical thermogravimetric (TG) curve and the first derivative of the weight loss (DTG) plot for $Al_2(SO_4)_3{\cdot}18H_2O$ salt. The TG curve and DTG plot are indicated as solid and dotted lines, respectively. The TG–DTG can be interpreted as follows: the aluminum sulfate hydrate decomposition takes place in several steps. The first three major steps are dehydration reactions in which eighteen moles of water is lost. In the range of 40–90°C, only a small weight loss is observed (about 6%). This is due to the fact that not all the water is released. As the temperature increases above 90°C, the coarse aluminum sulfate hydrate particles shatter, releasing water vapor. This is manifested by the fast weight loss on the TG curve of aluminum sulfate hydrate (≈24.5% between 90 and 151°C). Up to the end temperature of the third DTG peak (380°C), the cumulative weight loss of the sample was 46.5%, which approached the theoretical weight loss from the conversion of $Al_2(SO_4)_3{\cdot}18H_2O$ to $Al_2(SO_4)_3$ (48.6%). The formation of aluminum sulfate occurs when the temperature was between 706°C and 785°C. The weight loss increased with increasing the treatment temperature and the formation of $Al_2O(SO_4)_2$ is observed at temperatures between 785°C and 800°C (0.83 moles of SO_4 leaves the aluminum sulfate at 795°C). The theoretical weight loss due to the conversion of $Al_2(SO_4)_3{\cdot}18H_2O$ to $Al_2O(SO_4)_2$ is 60.6%. The last major step includes the sulfate ions decomposition to sulfur oxide vapor. The DTG peak with maxima at ≈808°C (about 70.7% weight loss) of sample is due to γ-Al_2O_3 phase formation. The loss of mass continued until approximately 900°C (about 84.7% weight loss), where α- Al_2O_3 is formed.

The XRD patterns of the final products of alum salt calcination at 785 and 795°C for 3 h are presented in Figure 2. The spectra relative to the powder obtained after calcination at 785°C show that it is polycrystalline. The diffraction peaks present in the XRD diffractogram are identical to those of the aluminium sulphate ($Al_2(SO_4)_3$) reference pattern (JCPDS Card number 01-077-0066). When the calcination temperature was increased from 785 to 795°C (Figure 2), the intensity of the aluminium sulphate phase peaks decreased, and several disappeared. At 795°C, the XRD results, combined with the FTIR results, indicate that the aluminium sulphate phase was present but at a lower amount than at 785°C. The weak peak intensities of the substance produced at 795°C reveal that a large amount of it was poorly crystallised. Matori et al. have found that the $Al_2(SO_4)_3$ phase lost its bonding and crystallinity after $Al_2(SO_4)_3{\cdot}18H_2O$ was calcined at 900°C [11]. However, the persistence and shape of the XRD peak at the $2\theta = 44.07^\circ$ position suggests that the nucleation of the γ-alumina phase had begun. The correlation between the XRD spectrum and the FTIR results obtained for the powder calcined at 795°C suggests that the $Al_2O(SO_4)_2$ metastable phase of the chemical decomposition of aluminium sulphate

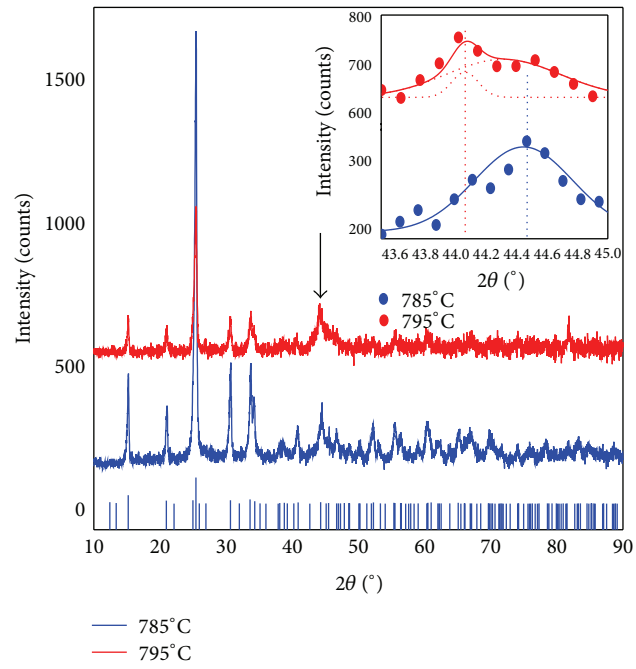

FIGURE 2: XRD patterns of the final products of alum salt calcination at 785 and 795°C for 3 h.

hydrate exhibits the rhombohedral structure of the aluminium sulphate present at this temperature.

The structural characterisation of the deposited specimen by the simple ultrasonic spray pyrolysis technique using the white solid formed after calcining the initial $Al_2(SO_4)_3{\cdot}18H_2O$ precursor at 795°C for 3 h in the spraying solution and annealed at two different temperatures during 1 hour is reported in Figure 3 ((a) 700°C and (b) 650°C). The XRD diffractogram relative to the coating treated by a 700°C-1 h heat treatment (Figure 3(a)) reveals the coexistence of zinc oxide and zinc aluminate. All peaks are well defined, indicating the highly crystalline nature of the phases present in the sample. Every diffraction peak of all phases is in good agreement with the standard diffraction patterns of hexagonal ZnO and cubic $ZnAl_2O_4$ spinel structures according to JCPDS card numbers 00-036-1451 and 00-001-1146, respectively. Table 1 displays XRD data of $ZnO/ZnAl_2O_4$ films. It shows typical polycrystalline hexagonal ZnO structures. The (002) peak has the highest intensity. Characteristics of $ZnAl_2O_4$ were also presented.

The lattice constants can be calculated using the following formulas:

$$d_{hkl} = \frac{1}{\sqrt{4\left(h^2 + k^2 + hk\right)/3a^2 + \left(l^2/c^2\right)}}, \qquad d_{hkl} = \frac{a}{\sqrt{h^2 + k^2 + l^2}}, \tag{1}$$

where a and c are the lattice constants and d_{hkl} is the crystalline surface distance for hkl indices. With the data in Table 1, the lattice constants of the ZnO and $ZnAl_2O_4$ films were calculated to be $a = b = 3.248$ Å, $c = 5.208$ Å and

Table 1: X-ray diffraction data for $ZnO/ZnAl_2O_4$ nanocomposite films (annealed at 700°C).

Pos. [°2Th.]	FWHM [°2Th.]	Identified planes (*hkl*)	d_{hkl} (Å)	Relative intensity (%)
31.3057	0.8839	220 $ZnAl_2O_4$	2.857	19.08
31.8155	0.1537	100 ZnO	2.813	31.48
34.5118	0.2024	002 ZnO	2.599	100.00
36.3725	0.2267	101 ZnO	2.470	53.29
36.8650	0.7104	311 $ZnAl_2O_4$	2.438	30.54
44.8092	0.6298	400 $ZnAl_2O_4$	2.023	2.24
47.6504	0.3149	102 ZnO	1.909	9.37
55.6419	0.6298	422 $ZnAl_2O_4$	1.652	3.65
56.7192	0.2362	110 ZnO	1.623	9.83
59.3661	0.6298	511 $ZnAl_2O_4$	1.557	6.27
62.9704	0.3149	103 ZnO	1.476	8.90
65.2577	0.4723	440 $ZnAl_2O_4$	1.430	9.10
68.0799	0.2880	112 ZnO	1.376	5.60

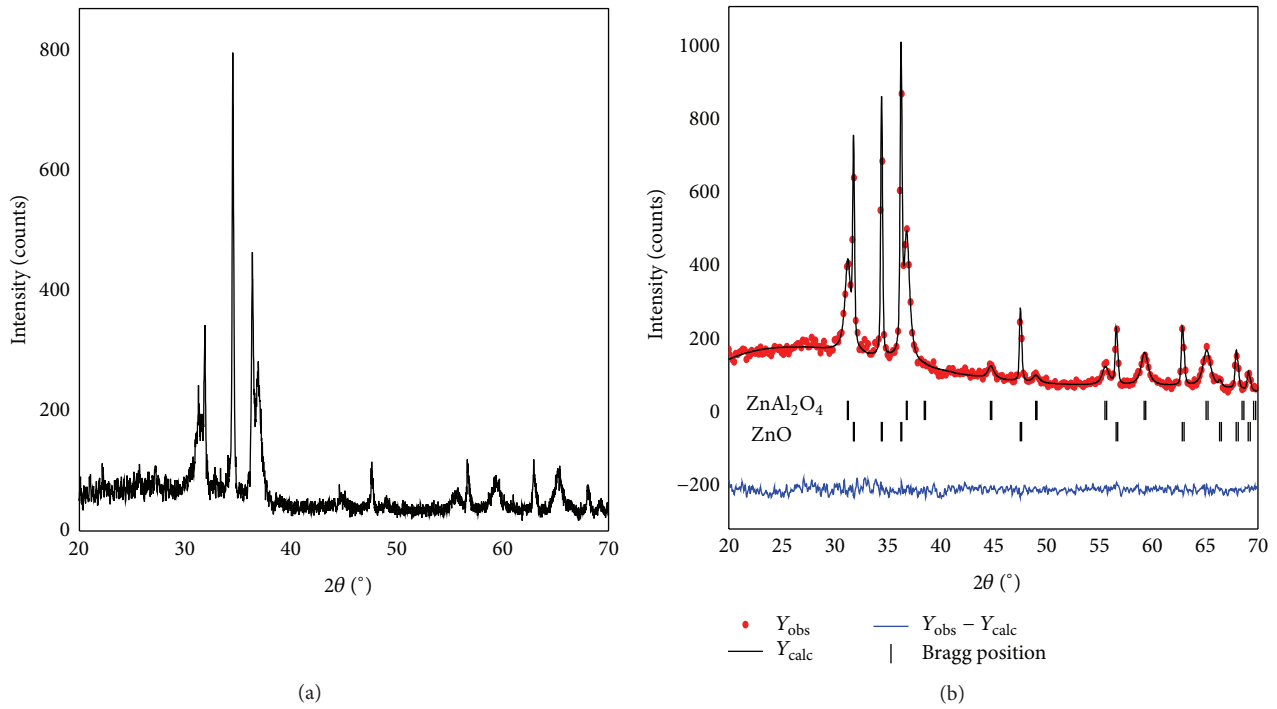

Figure 3: Typical XRD pattern of the $ZnO/ZnAl_2O_4$ nanocomposite films annealed during 1 h at (a) 700°C and (b) 650°C.

8.087 Å, respectively, and the reported values are $a = b = 3.249$ Å, $c = 5.207$ Å and 8.062 Å, respectively, according to the JCPDS data. This close agreement indicates the phase purity of the two oxides obtained.

Information on the crystallite size (D) for the films (i.e., $ZnO/ZnAl_2O_4$) was obtained from the full width at half maximum of the diffraction peaks using the Scherrer formula:

$$D = \frac{0.94\lambda}{\beta_{(hkl)} \cos \theta_{(hkl)}}, \quad (2)$$

where λ, $\theta(hkl)$, and $\beta(hkl)$ are the X-ray wavelength (0.15418 nm), Bragg diffraction angle, and line width at half maximum, respectively. This formula is not limited by the preferential orientation and is valid for an ordinary XRD profile. To improve the statistics, the most intense peaks in the profiles were chosen to determine the crystallite size.

The average crystallite sizes of ZnO and $ZnAl_2O_4$ were estimated to be 43 nm and 12 nm, respectively.

Rietveld refinement verified the formation of the $ZnO/ZnAl_2O_4$ composite films after also an annealing at 650°C for 1 h and is reported in Figure 3(b). Excellent

agreement is observed in terms of the peak positions and intensities between the theoretical and observed data, as depicted in Figure 3(b). The lattice parameters obtained from the Rietveld analysis of the ZnO and $ZnAl_2O_4$ structures are $a = b = 3.250$ Å, $c = 5.208$ Å and 8.097 Å, respectively, and the reported values are $a = b = 3.250$ Å, $c = 5.207$ Å and 8.087 Å, respectively, according to the JCPDS data. This close agreement indicates the phase purity of the two oxides obtained. The average crystallite sizes of ZnO and $ZnAl_2O_4$ were estimated to be 47 nm and 13 nm, respectively.

The relative crystallinity of each phase in the oxides mixture can be estimated by counting software diffractograms XRD (X'Pert HighScore). This estimation for the deposited system annealed at 650°C during 1 hour, for example, is of 60% for ZnO phase and 40% for $ZnAl_2O_4$ one.

In accordance with the X-ray diffraction analysis of the spraying product, the FTIR results of the deposited specimen heat treated at 700°C during 1 h (see Figure 4) demonstrate the presence of $ZnO/ZnAl_2O_4$ mixed compounds. The absorption peaks located at 675, 557, and 502 cm^{-1} are characteristic of the regular spinel structure with octahedrally coordinated aluminium centres only [12]. The absorption peak located at 431 cm^{-1}, corresponding to the Zn–O vibration frequency, is clearly represented, which is in agreement with the results obtained by XRD, and is significant red shifted compared with that of bulk ZnO manufactured via the French process (437.33 cm^{-1}) [13].

To probe with a fine way the present elements in our system as well as their chemical environment, the X-ray photoelectron spectroscopy (XPS) technique was employed. Indeed, the correlation of the different core levels binding energy positions with compounds properties which can be present in the film, the variations in binding energies, or chemical shifts of the photoelectron lines in the experimental curves reflect the modifications of the average atomic potential undergone by these electrons depending on the chemical bonds involved. This has been extremely useful in many studies. The sputtering of the sample surface in comparison with its initial surface induces changes in the binding displacement which refer directly to the preparation and preservation of the specimen. The film surface sputter cleaning step was inside the XPS chamber and XPS analyses were investigated both on the as-deposited and removable surface specimens. The XPS survey spectrum of the as-deposited coating (heat treated at 700°C for 1 h) reported in Figure 5 indicates the presence of Zn, O, and Al elements. However, some carbon and sulfur are incorporated in the as-deposited film and with more smaller quantities after a surface sputtering.

Figure 6(a) shows the XPS survey spectra of the as-deposited and sputter-cleaned (after 2 min, Ar^+ sputtering (~2 nm)) films. The quantitative analysis indicates that the surface atomic composition percentages of Zn, Al, and O change from 15.3, 14.6, and 53.4 at % to 16.5, 18.0, and 57.3 at %, respectively, after sputter cleaning the surface. These results are in good consistence with the expected theoretical values of Zn, Al, and O of the $ZnAl_2O_4$ and ZnO compounds, included in the general concentrations, assumed to other

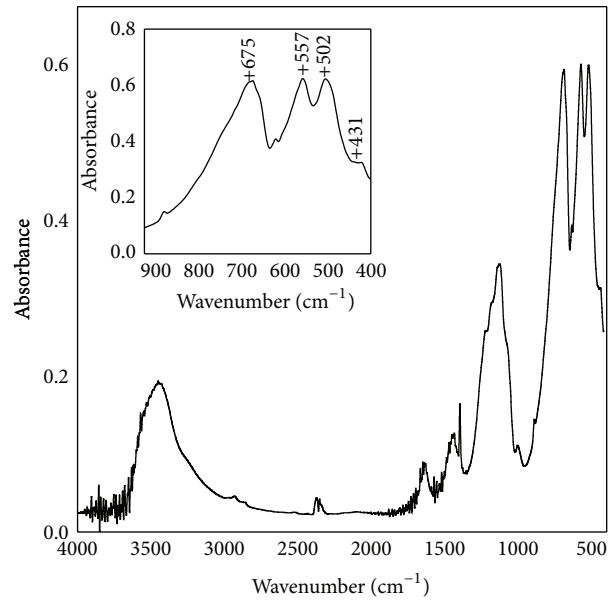

Figure 4: FTIR absorption spectrum of the $ZnO/ZnAl_2O_4$-deposited USP system and heat treated at 700°C for 1 h.

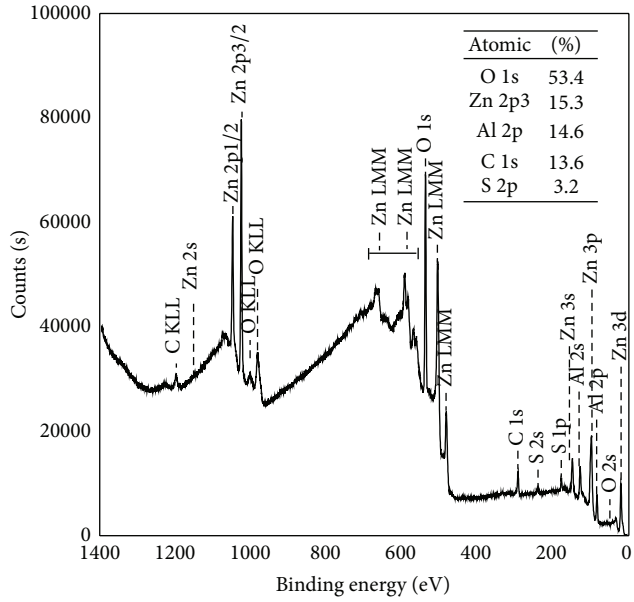

Figure 5: XPS survey spectrum of the as-deposited $ZnO/ZnAl_2O_4$ film annealed at 700°C for 1 h.

negligible oxygen configurations like the C–O contaminant one. The observed quantitative at. % concentrations of the Zn, Al, and O principal elements are in good agreement with the XRD analysis, where we have demonstrated the formation of a cubic crystalline phase of the $ZnAl_2O_4$ and wurtzite ZnO phase [14].

An important factor regarding the surface property of oxides is the occurrence of preferential segregation of one ion over another on the surface leading to a difference between the bulk and surface composition and in turn on catalytic

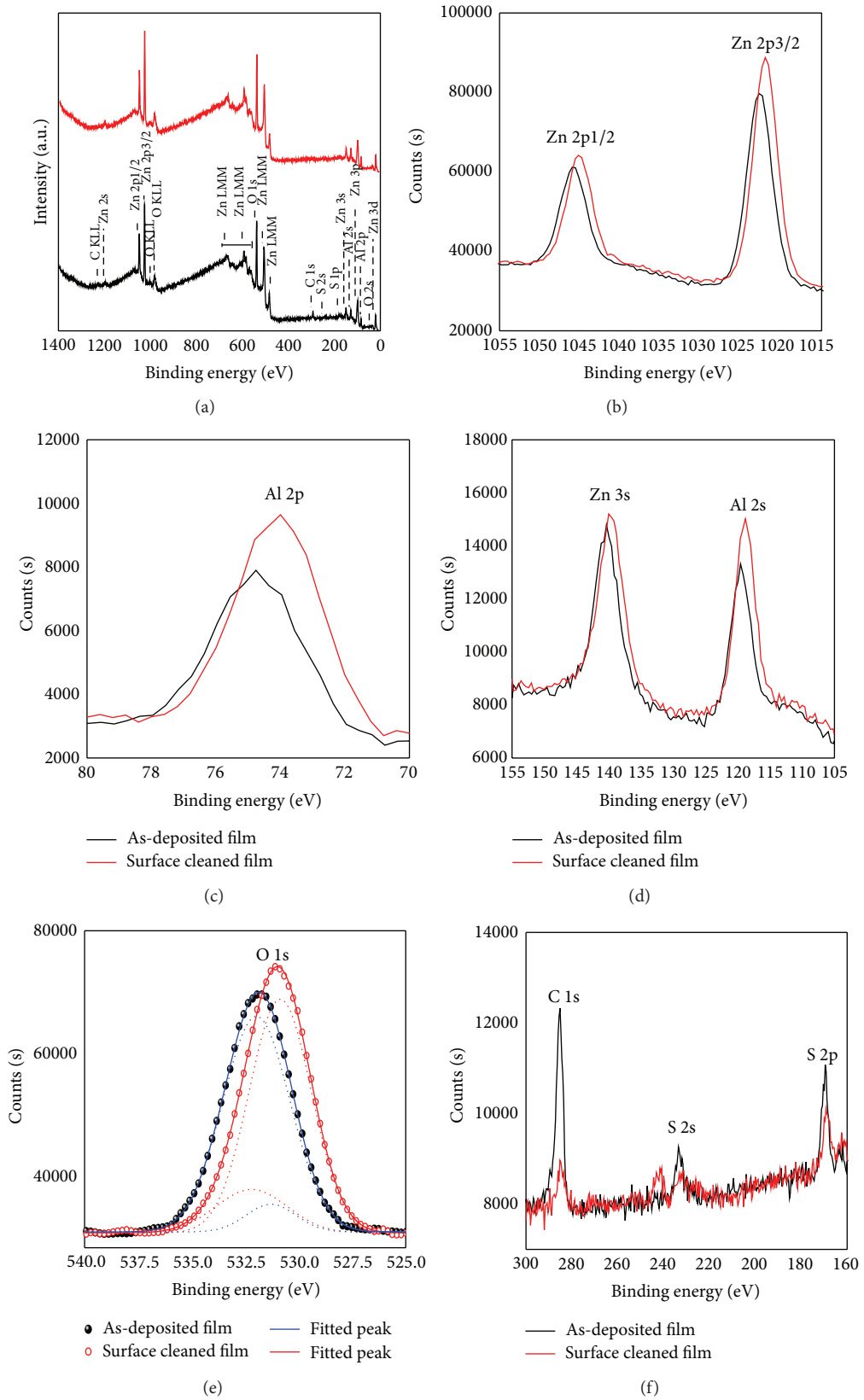

FIGURE 6: XPS survey spectra of the $ZnO/ZnAl_2O_4$ as-deposited (black line) and sputter-cleaned (red line) films treated at 700°C for 1 h (a), Zn 2p XPS spectrum (b), Al 2p XPS spectrum (c), Al 2s and Zn 3s XPS spectrum (d), O 1s XPS spectrum (e), and C 1s, S 2p, and S 2s XPS spectrum (f) of the samples.

properties. The atomic ratio of elements Zn/Al of the as-deposited film is about 1.04 : 1 and that of 2 min sputter-cleaned film is 0.91 : 1, deviating from the theoretical value of 1 : 1 calculated from the chemical formula of $ZnO/ZnAl_2O_4$. This result shows that the surface Zn/Al atomic composition is somewhat different from the bulk composition.

Figure 6(b) shows the XPS spectra in the Zn 2p region for these samples (as-deposited and sputter-cleaned thin film). The Zn 2p core level spectrum for thin film shows a doublet, whose binding energies are 1022.7 and 1045.9 eV (1022.0 and 1045.2 eV for the sputter-cleaned), which can be identified as the Zn 2p3/2 and Zn 2p1/2 lines, respectively. The binding energy differences between the two lines are 23.2 eV (23.2 eV for the sputter-cleaned), which is comfortably lying close to the standard reference value of ZnO [15]. The Zn 2p3/2 and Zn 2p1/2 binding energy positions and binding energy difference, calculated from XPS analysis, reveal the oxidation of the Zn atoms to the Zn^{2+} chemical state. Recorded to the Zn^{2+} 2p doublet collected before the surface ion-bombardment, a similar line shapes but a decrease in intensity and a minor shift in binding energy positions were detected, which indicates that the environment of Zn^{2+} at the top surface is slightly different from Zn^{2+} underneath it [16].

A high resolution XPS scan of the Al 2p peak reveals the nature of the aluminum bonding. Figure 6(c) shows the comparison of the Al 2p peaks for the sample before and after Ar^+ sputter cleaning for 2 min. The center of the peak shifts from 74.7 to 74.0 eV. The binding energy of the Al 2p signal is compatible with the presence of Al^{3+} species.

Figure 6(d) shows the XPS spectra in the Al 2s region for these samples (as-deposited and sputter-cleaned thin film). There is no considerable shift in Al 2s binding energy value centered around 119.5 and 118.8 eV for the as-deposited and sputter-cleaned thin film, respectively, indicating the presence of Al^{3+} on the surface. For the as-deposited film, no change in line shape was observed for Al^{3+} except for a decrease in intensity and a minor shift in binding energy, which shows that the environment of Al^{3+} at the top surface is slightly different from Al^{3+} underneath it. The same trend was observed for Zn 3s peak at 140.3 eV and 140.0 eV for the as-deposited and sputter-cleaned thin film, respectively.

Kim et al. reported that when Al-doped ZnO epitaxial layer is prepared and analysed by XPS, the strong O 1s peak at 530.6 eV is a characteristic of O^{2-} ions on the wurtzite structure of a hexagonal Zn^{2+} ion array, and the weak O 1s peak at 532.0 eV is characteristic of a nonstoichiometric Al–O phase [17].Chen et al., in an investigation of XPS and AES of Al-doped ZnO, reported that the three distinct components of O 1s can be attributed to the presence of loosely bound oxygen on the ZnO surface (532.4 eV), O^{2-} ions in the oxygen deficient regions within the ZnO (531.25 eV), and O^{2-} ions on the wurtzite structure of the hexagonal Zn^{2+} ion array (530.15 eV), respectively [18]. The deconvolution of the XPS spectra of the O 1s spectrum is shown in Figure 6(e). The O 1s core level spectrum of as-deposited film seems to be asymmetrical and can be best fitted using two Gaussian curves at 531.28 (FWHM 2.7) and 531.97 (FWHM 3.69) and may be attributed to the oxygen of ZnO crystal lattice [19] and oxygen of $ZnAl_2O_4$ [15], respectively. The O 1s core level spectrum of sputter-cleaned thin film can be best fitted using two Gaussian curves at 530.86 (FWHM 3.41) and 532.19 eV (FWHM 3.93). In case of sputter-cleaned film, the intensity at 532.2 eV binding energy decreases dramatically whereas the intensity of 532.19 eV peak increases.

Figure 6(f) shows the area of the survey scan in the proximity of the C 1s peak at 285.1 eV, S 2s, and S 2p regions of the (as-deposited and sputter-cleaned) coating annealed at 700°C for 1 h. A significant diminution in the intensity of the carbon line seen in the relative curve to the surface film after Ar^+ sputtering is characteristic of the purity of the bulk specimen from the carbon specie contamination. Tuan et al. explain this observation by the total reaction of the metal-organic precursor molecules and the desorbing of the carbon-containing ligands from the surface, so the peak in the as-deposited film spectrum is probably because the adventitious hydrocarbons apparently built up on the sample during the transfer through air [20]. Some sulfur content is detected in the as-deposited thin film, which becomes negligible after sputter cleaning of the film. The low sulfur content of the deposited film is likely due to decomposition of the aluminum oxide sulfate ($Al_2O(SO_4)_2$) precursor.

In this study, the modified Auger parameter method [15] (i.e., modified Auger parameter = α' = binding energy of the major photoelectron line plus the kinetic energy of the major Auger line for the element of interest) was used to determine the chemical state of zinc. It is known that the α' values located at 2010 and 2014 eV are characteristic of the oxidation state (Zn^{2+}) and metallic state (Zn^0), respectively [15]. For as prepared and sputter-cleaned $ZnO/ZnAl_2O_4$ films, the shifts of the α' are given in Table 2. That the α' values kept constant at ~2010.2 eV, being far from 2014 eV, indicates the existence of Zn^{2+} [21]. The calculated modified Auger parameter values for zinc oxide and $ZnO/ZnAl_2O_4$ system are identical but differed from the calculated value for the zinc aluminate by only 0.6 eV, as can be observed. This difference is usually not considered very pronounced and the differentiating between ZnO and $ZnO/ZnAl_2O_4$ and/or $ZnAl_2O_4$ becomes not possible and exhibits other data than α' values alone. A similar approach (rend) and deduction were reported by Strohmeier et al. to distinguish between ZnO and $Zn(OH)_2$ and/or $ZnAl_2O_4$ in their studied zincated disc, where the difference between the α' values obtained for these compounds was 0.4 eV [22]. However, the O ls values determined for the sputter-cleaned $ZnO/ZnAl_2O_4$ system and $ZnAl_2O_4$ material are equals and up to one electron volt in comparison with that of ZnO oxide. As can be seen from Table 2, the O 1s binding energy shows a chemical shift of 1.7 eV between $ZnO/ZnAl_2O_4$ (as-deposited film) and ZnO.

4. Conclusion

In this study, a $ZnO/ZnAl_2O_4$ system was successfully obtained from an inexpensive aluminium sulphate hydrate salt as the Al metal source by ultrasonic spray pyrolysis. The $Al_2(SO_4)_3{\cdot}18H_2O$ thermal decomposition product after calcination at 795°C for 3 h in air atmosphere combined with $ZnCl_2{\cdot}2H_2O$ salt in distilled water constitutes an efficient

Table 2: XPS binding energies (eV) for zinc reference compounds and $ZnO/ZnAl_2O_4$ system (annealed at 700°C). [a]As-deposited film, [b]surface cleaned film, and Auger values in kinetic energy (KE). Zinc Auger parameter = binding energy Zn 2p3/2 + kinetic energy Zn LMM.

Sample	Zn 2p3/2	Zn LMM Auger	Zn Auger parameter	Zn 2p1/2	Zn 3p	Zn 3s	O 1s	Al 2p	Al 2s	S 2p	S 2s	C 1s
ZnO [6]	1021.5	988.6	2010.1	1044.6	88.6	139.5	530.2	/	/	/	/	285.1
$ZnAl_2O_4$ [6]	1022.0	987.5	2009.5	1045.1	89.4	140.3	531.3	74.5	119.3	/	/	285.1
$ZnO/ZnAl_2O_4$[a] Iaiche et al.	1022.7	987.4	2010.1	1045.9	89.5	140.3	531.9	74.7	119.5	233.5	169.5	285.1
$ZnO/ZnAl_2O_4$[b] Iaiche et al.	1022.0	988.2	2010.2	1045.2	89.2	140.0	530.9	74.0	118.8	/	169.2	285.1

spraying solution. A relatively low substrate temperature (570°C) for the $ZnAl_2O_4$ formation was employed. The preparation conditions permit the formation of a nanometric $ZnAl_2O_4$ phase. The structures of the synthesised $ZnO/ZnAl_2O_4$ films were confirmed by XRD, FTIR, and X-ray photoelectron spectroscopy. XPS spectra of the major Zn, Al, and O photoelectron lines and the major X-ray induced Zn LMM Auger lines for $ZnO/ZnAl_2O_4$ are presented.

Conflict of Interests

The authors declare that there is no conflict of interests regarding the publication of this paper.

Acknowledgments

This work was supported in part by the National Project Research (PNR) and LASPI^{2}A Laboratory of Khenchela University, Algeria.

References

[1] M. Zawadzki, "Synthesis of nanosized and microporous zinc aluminate spinel by microwave assisted hydrothermal method (microwave-hydrothermal synthesis of $ZnAl_2O_4$)," *Solid State Sciences*, vol. 8, no. 1, pp. 14–18, 2006.

[2] K. Kumar, K. Ramamoorthy, P. M. Koinkar, R. Chandramohan, and K. Sankaranarayanan, "A novel in situ synthesis and growth of $ZnAl_2O_4$ thin films," *Journal of Crystal Growth*, vol. 289, no. 1, pp. 405–407, 2006.

[3] T. R. Kumar, N. C. S. Selvam, C. Ragupathi, J. L. Kennedy, and J. J. Vijaya, "Synthesis, characterization and performance of porous Sr(II)-added $ZnAl_2O_4$ nanomaterials for optical and catalytic applications," *Powder Technology*, vol. 224, pp. 147–154, 2012.

[4] T. El-Nabarawy, A. A. Attia, and M. N. Alaya, "Effect of thermal treatment on the structural, textural and catalytic properties of the ZnO-Al_2O_3 system," *Materials Letters*, vol. 24, no. 5, pp. 319–325, 1995.

[5] M. S. Hadnadev-Kostić, T. J. Vulić, D. B. Zorić, and R. P. Marinković-Nedučin, "The influence of the UV irradiation intensity on photocatalytic activity of ZnAl layered double hydroxides and derived mixed oxides," *Chemical Industry & Chemical Engineering Quarterly*, vol. 18, no. 2, pp. 295–303, 2012.

[6] B. R. Strohmeier and D. M. Hercules, "Surface spectroscopic characterization of the interaction between zinc ions and γ-alumina," *Journal of Catalysis*, vol. 86, no. 2, pp. 266–279, 1984.

[7] K. S. Brady, J. M. Bigham, W. F. Jaynes, and T. J. Logan, "Influence of sulfate on Fe-oxide formation: comparisons with a stream receiving acid mine drainage," *Clays & Clay Minerals*, vol. 34, no. 3, pp. 266–274, 1986.

[8] J. Pysiak and B. Pacewska, "Investigation of thermal decomposition of solids," *Journal of Thermal Analysis*, vol. 29, no. 5, pp. 879–894, 1984.

[9] N. H. Nickel and K. Fleischer, "Hydrogen local vibrational modes in zinc oxide," *Physical Review Letters*, vol. 90, no. 19, Article ID 197402, 4 pages, 2003.

[10] T. J. Truex, R. H. Hammerle, and R. A. Armstrong, "The thermal decomposition of aluminium sulfate," *Thermochimica Acta*, vol. 19, no. 3, pp. 301–304, 1977.

[11] K. A. Matori, L. C. Wah, M. Hashim, I. Ismail, and M. H. Mohd Zaid, "Phase transformations of α-alumina made from waste aluminum via a precipitation technique," *International Journal of Molecular Sciences*, vol. 13, no. 12, pp. 16812–16821, 2012.

[12] A. K. Adak, A. Pathak, and P. Pramanik, "Characterization of $ZnAl_2O_4$ nanocrystals prepared by the polyvinyl alcohol evaporation route," *Journal of Materials Science Letters*, vol. 17, no. 7, pp. 559–561, 1998.

[13] K. Bouzid, A. Djelloul, N. Bouzid, and J. Bougdira, "Electrical resistivity and photoluminescence of zinc oxide films prepared by ultrasonic spray pyrolysis," *Physica Status Solidi A*, vol. 206, no. 1, pp. 106–115, 2009.

[14] L. Zhang, J. Yan, M. Zhou, Y. Yang, and Y.-N. Liu, "Fabrication and photocatalytic properties of spheres-in-spheres $ZnO/ZnAl_2O_4$ composite hollow microspheres," *Applied Surface Science*, vol. 268, pp. 237–245, 2013.

[15] J. F. Moulder, W. F. Strickle, P. E. Sobol, and K. D. Bomben, *Handbook of X-Ray Photoelectron Spectroscopy*, ULVAC-PHI, Chigasaki, Japan, 1992.

[16] A. Vij, S. Gautam, S. O. Won, A. Thakur, I.-J. Lee, and K. H. Chae, "X-ray photoelectron spectroscopy of $Zn_{0.98}Cu_{0.02}O$ thin film grown on ZnO seed layer by RF sputtering," *Materials Letters*, vol. 88, pp. 51–53, 2012.

[17] H.-K. Kim, T.-Y. Seong, K.-K. Kim, S.-J. Park, Y. S. Yoon, and I. Adesida, "Mechanism of nonalloyed Al ohmic contacts to n-type ZnO:Al epitaxial layer," *Japanese Journal of Applied Physics*, vol. 43, no. 3, pp. 976–979, 2004.

[18] M. Chen, X. Wang, Y. H. Yu et al., "X-ray photoelectron spectroscopy and auger electron spectroscopy studies of Al-doped ZnO films," *Applied Surface Science*, vol. 158, no. 1, pp. 134–140, 2000.

[19] G.-S. Kim, S. G. Ansari, H.-K. Seo, Y.-S. Kim, O.-B. Yang, and H.-S. Shin, "Hydrothermal growth of ZnO on annealed electrodeposited titanate film: influence of zinc nitrate and methenamine," *Applied Surface Science*, vol. 253, no. 17, pp. 7197–7202, 2007.

[20] A. C. Tuan, J. D. Bryan, A. B. Pakhomov et al., "Epitaxial growth and properties of cobalt-doped ZnO on α-Al_2O_3 single-crystal substrates," *Physical Review B—Condensed Matter and Materials Physics*, vol. 70, no. 5, Article ID 054424, 9 pages, 2004.

[21] M. Xue and Q. Guo, "Layer-by-layer growth of polar MgO(111) ultrathin films," *The Journal of Chemical Physics*, vol. 127, no. 5, Article ID 054705, 2007.

[22] B. R. Strohmeier, W. T. Evans, and D. M. Schrall, "Preparation and surface characterization of zincated aluminium memory-disc substrates," *Journal of Materials Science*, vol. 28, no. 6, pp. 1563–1572, 1993.